COUPLING EULER AND POTENTIAL METHODS FOR THE CALCULATION OF HELICOPTER ROTORS IN UNSTEADY FORWARD FLIGHT

D. Wehr, L. Zerle, S. Wagner
Institut für Aero- und Gasdynamik, Universität Stuttgart
70550 Stuttgart, Germany

Abstract

For the simulation of multi-bladed rotors in hover and forward flight the influence of the preceding blades has to be taken into account for the correct calculation of all vortex-related features of the flow field. This can be done by applying a local angle of attack correction or transpiration velocity at the blade which are obtained by a prescribed wake model. In the present paper another approach is made since a free wake model is used to provide the boundary conditions at the outer limits of the Euler grid in order to produce and transport the wake into the calculation domain. It is shown that this procedure is able to capture the wake correctly. Thus, the grid can be limited to one blade so that there is no need to cover the whole rotor by a closed grid. This leads to considerable savings in storage and computational time. Results are presented for the ONERA PF1 three-bladed model rotor and show good agreement with the experiment.

List of Symbols

A, B, C	jacobian matrices of fluxes
c_p	pressure coefficient
c_n	normal force coefficient
D	diagonal matrix
$\vec{E}, \vec{F}, \vec{G}$	flux vectors in ξ, η, ζ direction
e	specific total energy
$\bar{\bar{e}}$	specific total disturbance energy
I	identity matrix
i, j, k	grid index in ξ, η, ζ direction
$\vec{K}$	centrifugal and Coriolis force vector
L	lower triangular matrix
LHS	matrix of left hand side
M_t	tip mach number
M_∞	freestream mach number
n	index of time step
p	pressure
p_∞	freestream pressure
R	rotor radius
$\overrightarrow{RHS}$	right hand side
r	radius
S	jacobian matrix of $\vec{K}$
s	velocity of sound
U	upper triangular matrix
u, v, w	absolute velocities
$\bar{U}, \bar{V}, \bar{W}$	contravariant disturbance velocities
$\bar{u}, \bar{v}, \bar{w}$	disturbance velocities
V	cell volume
x, y, z	cartesian coordinates
$\dot{x}, \dot{y}, \dot{z}$	grid velocities
α	pitch angle
α_s	shaft angle
β	flap angle
κ	isentropic exponent
μ	index of Newton iteration
ω	angular velocity
$\vec{\Phi}$	vector of conservative variables
Ψ	azimuth angle
ρ	density
σ	spectral radius
τ	time
ξ, η, ζ	body fitted coordinates
ξ_x, ξ_y, ξ_z	surface normal vector
$\tilde{\xi}_x$ etc.	$V \cdot \xi_x$

Introduction

A key component for the realistic simulation of helicopter flight is the accurate calculation of the aerodynamics of the rotor. Today blade element theory together with prescribed i. e. fixed wake geometries are still widely used in industry for performance prediction, analysis of stability, trim and flight mechanics.

Important features of rotor flow, such as blade-vortex interactions, shock movement on the advancing blade at high advance ratios and dynamic stall on the retreating side are not captured by these methods, thus necessitating the development and use of more sophisticated techniques.

For the accurate treatment of rotor flow, in the last few years Euler and Navier–Stokes methods have been developed for steady and unsteady flight conditions. However, they make high demands on computational speed and memory due to the required grid size. A large extension of the net is necessary for the correct calculation of the wake, which has to be as undisturbed by the farfield boundary as possible. The correct simulation of multibladed rotors in forward flight is strongly dependent on the way in which the wake is handled. If the use of a computational domain enclosing all blades in order to capture the wake without further modelling is not desired or possible, there are several possibilities to take the wake influence into account. Firstly, the local angle of attack at the blade sections is rotated by the induced angles due to the other blades. Secondly, a transpiration boundary condition is applied on the blade surface using induced velocities. The alternative to these two methods is prescription of initial and farfield boundary conditions by a fixed or free wake model. This possibility was already successfully applied to Euler calculations of steady rotor flows by Hertel [2] and an extension to unsteady flows is accomplished in the present paper.

Applied methods

Euler solver

The Euler equations are formulated in body-fitted coordinates as

$$\frac{\partial\vec{\Phi}}{\partial\tau}+\frac{\partial\vec{E}}{\partial\xi}+\frac{\partial\vec{F}}{\partial\eta}+\frac{\partial\vec{G}}{\partial\zeta}=\vec{K}\quad , \qquad (1)$$

where

$$\vec{\Phi}=V\cdot\left(\rho,\rho\bar{u},\rho\bar{v},\rho\bar{w},\bar{\bar{e}}\right) \qquad (2)$$

is the vector of conservative variables multiplied by the cell volume. Velocity and energy are given in terms of disturbance velocities in the rotating frame of reference, which is attached to z-axis representing the rotor shaft, as

$$\begin{aligned}\bar{u} &= u-\omega y && (3)\\ \bar{v} &= v+\omega x && (4)\\ \bar{w} &= w && (5)\\ \bar{\bar{e}} &= e-\rho\omega\left(\bar{u}y-\bar{v}x\right)-\frac{\rho}{2}\left(\omega r\right)^2 && (6)\end{aligned}$$

The flux $\vec{E}$ is given by

$$\vec{E}=\begin{pmatrix}\rho\left[\overline{U}+\omega\left(y\bar{\xi}_x-x\bar{\xi}_y\right)\right]\\ \rho\bar{u}\left[\overline{U}+\omega\left(y\bar{\xi}_x-x\bar{\xi}_y\right)\right]+p\bar{\xi}_x\\ \rho\bar{v}\left[\overline{U}+\omega\left(y\bar{\xi}_x-x\bar{\xi}_y\right)\right]+p\bar{\xi}_y\\ \rho w\left[\overline{U}+\omega\left(y\bar{\xi}_x-x\bar{\xi}_y\right)\right]+p\bar{\xi}_z\\ \bar{\bar{e}}\left[\overline{U}+\omega\left(y\bar{\xi}_x-x\bar{\xi}_y\right)\right]+p\overline{U}-p\bar{\xi}_\tau\end{pmatrix} \qquad (7)$$

with

$$\bar{\xi}_\tau=V\left(\dot{x}\xi_x+\dot{y}\xi_y+\dot{z}\xi_z\right) \qquad (8)$$

representing the time derivative of the surface normal vector.

The source term $\vec{K}$ resulting from the transformation into the moving system, which contains the contributions of centrifugal and Coriolis forces can be written as

$$\vec{K}=\rho\omega\begin{pmatrix}0\\ \bar{v}\\ -\bar{u}\\ 0\\ 0\end{pmatrix}\quad . \qquad (9)$$

$\overline{U}$ is the contravariant disturbance velocity and is defined as

$$\overline{U}=\bar{u}\bar{\xi}_x+\bar{v}\bar{\xi}_y+w\bar{\xi}_z-\bar{\xi}_\tau \qquad (10)$$

The formulas for $\vec{F}$ and $\vec{G}$ are analogous to $\vec{E}$ substituting their respective metric terms and contravariant velocities $\bar{V}$, $\bar{W}$. Here $\bar{\xi}_x=V\cdot\xi_x$ is the product of the normal vectors of the cell-faces and the volume and $\dot{x}$, $\dot{y}$, $\dot{z}$ denote the grid velocities.

For the time integration the second order 3-point backward-difference scheme was chosen, which gives after semi-discretization the following implicit system of equations

$$\frac{3}{2}\frac{\vec{\Phi}^{n+1}-\vec{\Phi}^{n}}{\Delta\tau}-\frac{1}{2}\frac{\vec{\Phi}^{n}-\vec{\Phi}^{n-1}}{\Delta\tau}+ \vec{E}_\xi^{n+1}+\vec{F}_\eta^{n+1}+\vec{G}_\zeta^{n+1}-\vec{K}^{n+1}=0 \qquad (11)$$

For its solution, a Newton method was applied and led to

$$\underbrace{\left[\frac{\mathbf{I}}{\Delta\tau} + \frac{2}{3}\left(\mathbf{A}^{\mu}_{\xi} + \mathbf{B}^{\mu}_{\eta} + \mathbf{C}^{\mu}_{\zeta} - \mathbf{S}^{\mu}\right)\right]}_{\mathbf{LHS}} \Delta\vec{\Phi}^{\mu+1} =$$
$$\underbrace{-\left[\frac{\vec{\Phi}^{\mu} - \vec{\Phi}^{n}}{\Delta\tau} - \frac{1}{3}\frac{\vec{\Phi}^{n} - \vec{\Phi}^{n-1}}{\Delta\tau} + \frac{2}{3}\left(\vec{E}^{\mu}_{\xi} + \vec{F}^{\mu}_{\eta} + \vec{G}^{\mu}_{\zeta} - \vec{K}^{\mu}\right)\right]}_{\overrightarrow{RHS}} \tag{12}$$

where μ denotes the index of the subiteration within the time step and **A**, **B**, **C** and **S** are the jacobian matrices of the fluxes, respectively of the source term.

In [10] a Point-Gauss-Seidel method with an additive decomposition of the left-hand side matrix has been used for the solution of the arising system of equations, whereas for the present study the LUSGS (Lower-Upper Symmetric Gauss Seidel) implicit operator by Jameson and Yoon [3] has been implemented. It consists of an approximate factorization in lower **L**, diagonal **D** and upper matrices **U** of the form

$$\mathbf{LHS} = \mathbf{L}\cdot\mathbf{D}\cdot\mathbf{U} \tag{13}$$

With $\Delta_{\xi,\eta,\zeta}$ and $\nabla_{\xi,\eta,\zeta}$ as forward- and backward-differences in the 3 coordinate directions the matrices are defined as

$$\begin{aligned}\mathbf{L} &= \mathbf{I} + \gamma\Delta\tau\left(-\mathbf{A}^{-}_{ijk} + \nabla_{\xi}\mathbf{A}^{+} - \mathbf{B}^{-}_{ijk}\right. \\ &\quad \left. + \nabla_{\eta}\mathbf{B}^{+} - \mathbf{C}^{-}_{ijk} + \nabla_{\zeta}\mathbf{C}^{+}\right) \qquad (14)\\ \mathbf{D} &= \left[\mathbf{I} + \gamma\Delta\tau\left(\mathbf{A}^{+}_{ijk} - \mathbf{A}^{-}_{ijk} + \mathbf{B}^{+}_{ijk}\right.\right. \\ &\quad \left.\left. - \mathbf{B}^{-}_{ijk} + \mathbf{C}^{+}_{ijk} - \mathbf{C}^{-}_{ijk}\right)\right]^{-1} \qquad (15)\\ \mathbf{U} &= \mathbf{I} + \gamma\Delta\tau\left(\mathbf{A}^{+}_{ijk} + \Delta_{\xi}\mathbf{A}^{-} + \mathbf{B}^{+}_{ijk}\right. \\ &\quad \left. + \Delta_{\eta}\mathbf{B}^{-} + \mathbf{C}^{+}_{ijk} + \Delta_{\zeta}\mathbf{C}^{-}\right) \qquad (16)\end{aligned}$$

γ is 2/3 for the chosen time discretization, when other schemes are applied this factor has to be adapted on the LHS. A simplified calculation of the split matrices can be carried out using

$$\mathbf{A}^{\pm} = \frac{1}{2}\left(\mathbf{A} \pm \sigma_{\xi}\mathbf{I}\right), \tag{17}$$

where σ_{ξ} is the spectral radius of **A** multiplied by a factor $k \geq 1$

$$\begin{aligned}\sigma_{\xi} &= \left(\left|(u - \dot{x})\xi_x + (v - \dot{y})\xi_y + (w - \dot{z})\xi_z\right|\right. \\ &\quad \left. + s\sqrt{\xi_x^2 + \xi_y^2 + \xi_z^2}\right) k \qquad (18)\end{aligned}$$

Applying LUSGS to steady hypersonic flows, Rieger and Jameson [8] noted that diagonal dominance could be enhanced by substituting σ_{ξ} by its maximum of the currently computed point and its preceding respectively following neighbour for the **L** and **U** matrices:

$$\begin{aligned}\sigma^{-}_{\xi} &= \max\left(\sigma_{\xi_{i,j,k}}, \sigma_{\xi_{i-1,j,k}}\right) \qquad (19)\\ \sigma^{+}_{\xi} &= \max\left(\sigma_{\xi_{i,j,k}}, \sigma_{\xi_{i+1,j,k}}\right) \qquad (20)\end{aligned}$$

Though the unsteady formulation of the presented solver leads to the additional **I** on the main diagonal, experience showed that the modified calculation is advantageous in terms of robustness. Introducing the abbreviations

$$\begin{aligned}\sigma_L &= \sigma^{-}_{\xi_{i,j,k}} + \sigma^{-}_{\eta_{i,j,k}} + \sigma^{-}_{\zeta_{i,j,k}} \qquad (21)\\ \sigma_U &= \sigma^{+}_{\xi_{i,j,k}} + \sigma^{+}_{\eta_{i,j,k}} + \sigma^{+}_{\zeta_{i,j,k}} \qquad (22)\\ \sigma_D &= \frac{1}{2}\left(\sigma_L + \sigma_U\right) \qquad (23)\end{aligned}$$

eq. (14) - (16) can be written as

$$\begin{aligned}\mathbf{L} &= \mathbf{I}\left(1 + \gamma\Delta\tau\ \sigma_L\right) - \gamma\Delta\tau\cdot \\ &\quad \cdot\left(\mathbf{A}^{+}_{i-1,j,k} + \mathbf{B}^{+}_{i,j-1,k} + \mathbf{C}^{+}_{i,j,k-1}\right) (24)\\ \mathbf{D} &= \mathbf{I}\left[\left(1 + \gamma\Delta\tau\ \sigma_D\right)\right]^{-1} \qquad (25)\\ \mathbf{U} &= \mathbf{I}\left(1 + \gamma\Delta\tau\ \sigma_U\right) + \gamma\Delta\tau \\ &\quad \cdot\left(\mathbf{A}^{-}_{i+1,j,k} + \mathbf{B}^{-}_{i,j+1,k} + \mathbf{C}^{-}_{i,j,k+1}\right) (26)\end{aligned}$$

A closer inspection reveals that the diagonals of the 3 matrices consist only of scalar diagonal 5 × 5 submatrices, which means that only divisions are necessary for the solution, thus resulting in fewer operations than the Point-Gauss-Seidel algorithm where block matrix inversions have to be carried out. The following equation

$$\mathbf{L}\cdot\mathbf{D}\cdot\mathbf{U}\Delta\vec{\Phi}^{\mu+1} = -\Delta\tau\vec{RHS}^{\mu} \tag{27}$$

is therefore straightforward to be solved in three steps.

$$\begin{aligned}\Delta\vec{\Phi}^{*} &= \mathbf{L}^{-1}\left(-\Delta\tau\vec{RHS}^{\mu}\right) \qquad (28)\\ \Delta\vec{\Phi}^{**} &= \mathbf{D}^{-1}\Delta\vec{\Phi}^{*} \qquad (29)\\ \Delta\vec{\Phi} &= \mathbf{U}^{-1}\Delta\vec{\Phi}^{**} \qquad (30)\end{aligned}$$

It is even possible to eliminate the calculation of the flux jacobians and the subsequent multiplication with $\Delta\vec{\Phi}$ by applying a Taylor expansion to the fluxes.

$$\vec{E^{\pm}}^{*} = \vec{E^{\pm}}^{\mu} + \frac{\partial\vec{E}^{\pm}}{\partial\vec{\Phi}}\left(\vec{\Phi}^{*} - \vec{\Phi}^{\mu}\right) + O(|\Delta\vec{\Phi}^{2}|) \tag{31}$$

Now the matrix-vector products can be replaced by

$$\Delta\vec{E}^{\pm *} = \vec{E}^{\pm *} - \vec{E}^{\pm\mu} = \mathbf{A}^{\pm}\Delta\vec{\Phi}^{*} + O(|\Delta\vec{\Phi}^{2}|) \tag{32}$$

Using the homogeneous property

$$\vec{E}\left(\vec{\Phi}\right) = \mathbf{A}\vec{\Phi} \tag{33}$$

the following relation is approximatively valid:

$$\vec{E}^{\pm} \approx \frac{1}{2}\left(\mathbf{A} \pm \sigma_{\xi}\mathbf{I}\right)\vec{\Phi} = \frac{1}{2}\left[\vec{E}\left(\vec{\Phi}\right) \pm \sigma_{\xi}\vec{\Phi}\right] \tag{34}$$

Now the split fluxes can be determined by

$$\begin{aligned} \Delta\vec{E}^{+*} &= \frac{1}{2}\left[\vec{E}\left(\vec{\Phi}^{\mu} + \Delta\vec{\Phi}^{*}\right)\right. \\ &- \left.\vec{E}\left(\vec{\Phi}^{\mu}\right) + \sigma_{\xi}\Delta\vec{\Phi}^{*}\right] \qquad (35) \\ \Delta\vec{E}^{-**} &= \frac{1}{2}\left[\vec{E}\left(\vec{\Phi}^{\mu} + \Delta\vec{\Phi}^{**}\right)\right. \\ &- \left.\vec{E}\left(\vec{\Phi}^{\mu}\right) - \sigma_{\xi}\Delta\vec{\Phi}^{**}\right] \qquad (36) \end{aligned}$$

The experience described in [8] that the substitution of jacobians by flux differences did not influence the convergence rate in a negative manner can be confirmed for unsteady flow conditions, too.

The algorithm is completely vectorizable by choosing the sweep direction normal to planes defined by $i + j + k = const$ avoiding recursion in that way. The grid points have to be reordered and stored by diagonal planes. In that way, the vector length is also increased with respect to a i, j, k ordering. Depending on the computer architecture the implemented algorithm runs faster by a factor ranging from to 2 to 4 than the formerly used Point-Gauss-Seidel solver.

For the finite volume, cell centred scheme the evaluation of the fluxes at the cell faces, which appears on the RHS is done by an approximate Riemann solver due to Eberle [1] and its implementation for unsteady rotor–flows is described by Stangl in [9]. Application of a low dispersion scheme [4] results in third order spatial accuracy, being switched to first order upwind at discontinuities.

Potential method

For the generation of initial and boundary conditions an accurate method is needed in order to predict the wake-induced velocities correctly for arbitrary rotor configurations and forward flight conditions. Because of this requirement a free-wake method as given by Zerle and Wagner [11] was prefered to a prescribed wake. It is based on 3-dimensional linear potential flow and the solution is advanced in time by using the information of the former step by a procedure which consists of two parts. First, by imposing the no-slip boundary condition at the blade control points, the local vorticity strength at the panel can be calculated. Then, a displacement of the wake networks takes place, they are prolongated and newly positioned. Assuming a quasi steady potential flow and a frozen geometry system during the timestep the new flow field and wake geometry are determined at the end of the timestep.

The discretization of the blade consists of thin panels each covered with a vortex doublet ring. Using the blade-panel to blade-panel influence coefficient matrix at the end of the time step the panel doublet strength is computed.

Using sheets of quadriliteral ring vorticies (wake doublets) the wake is discretized. The vortex strength of the vortex filament between two adjacent doublets is calculated by balancing (subtracting) their strengths. At each new time step a new wake row is produced at the trailing edge, where the Kutta condition is applied. For wake movement and distorsion the influence of the freestream and every singularity is taken into account. Further details are contained in [11].

The output consists of lattices of blade and wake vortices and their respective strengths, which are shown in fig. 1 together with the outer boundaries of the Euler grid.

Postprocessing of vortex-lattice data

In order to produce input data suitable for the Euler solver, the vector of conservative flow variables has to be provided initially at the location of all cell centers and at the farfield boundary in the subsequent time-steps.

Since the vortex lattice with known doublet strengths is given, the vorticity strength of the single vortex filaments can be computed by adding up the doublet strengths of neighbouring rafters as well as spars of the blades and of the wake. Then the application of Biot–Savart's law to each spar and rafter of all the blade and wake vortices gives the induced velocities. In order to model the physical characteristics of a real vortex a suitable zero induction radius and an exponential damping factor are applied. Adding freestream and induced velocity the absolute velocity is determined. Density and specific total energy are computed under the assumption of isentropic flow. For the preservation of the third order scheme the generated data serves as input for the outer two cell rows.

Two revolutions were performed with a step-size of 15 degrees, which is sufficient for the generation of the older wake portion which is not in the vicinity of the blade. Then a third revolution was performed with 5 degrees, producing a finer lattice for the vortex system interacting more closely with the blade. At these angles the grid positioning and the evaluation at the cell centers on the outer boundaries took place. Since the data generation for every step of the Euler calculation (about .5 to 1 degree) would be prohibitive in terms of computation time and resulting input file size a linear interpolation between two subsequent steps of the vortex lattice was chosen for the provision of the time-dependent variations of the conservative flow variables for the Euler solver.

Results

Testcase

The selected test case was that of the ONERA PF1 3-bladed rotor with a tip Mach number .613 and an advance ratio of .4. The following pitch and flap variations as well as the shaft angle were applied:

$$\begin{aligned}\alpha &= 14.16^\circ + 0.43^\circ \cos\Psi(t) - 5.14^\circ \sin\Psi(t)\\ \beta &= 1.25^\circ - 5.12^\circ \cos\Psi(t) + 0.32^\circ \sin\Psi(t)\\ \alpha_s &= -12.4^\circ\end{aligned}$$

The grid used for the wake visualizations, which outer boundaries are shown in fig. 1 is made up of $197 \times 60 \times 48$ nodes.

Examination of the wake system

Within a closed computational domain Euler methods are able to capture the wake correctly as a part of the solution without the application of external wake models as reported by Kroll [6] or Krämer et al. [5] for steady rotor flows. For unsteady flows, like helicopter configurations in forward flight, the chimera technique consists of covering the whole computational domain with overlaid embedded grids thus ensuring the correct capturing of all wake influences. The single components (rotor-blades, fuselage, tail rotor) can interact exchanging the conservative variables on the overlapping boundaries, as has been demonstrated by Stangl [10]. However, this procedure puts high demands on available memory and computational time. Also some care is necessary to assure similar cell sizes in the regions where intergrid information transfer occurs, so that transport of vorticity is assured.

In the present paper the question is investigated if the wake-capturing feature can also be used to simulate the influence of preceding blades without the need for a domain enclosing the complete rotor only by imposing suitable conditions on the boundaries of the grid thus allowing for considerable savings in storage and CPU time.

For the visualization of the wake system several possibilties exist. For hover and axial translation cases, Krämer [4] used isolines of total pressure loss and circulation density in planes through the axis of rotation. Since in forward flight conditions it is difficult to define such planes of primary interest, in [10] isosurfaces of the absolute magnitude of the rotation vector were found to be adequate for the purpose of examining the main features of the flow as tip and inboard vortices, but also vortex sheets. Since a huge amount of data is involved in this analysis, only three azimuthal positons at $\Psi = 0^\circ, \ , 120^\circ, \ 240^\circ$ are shown here, which are sufficient to demonstrate the results of the coupling. They have been calculated on the original grid in order to obtain a more comprehensive insight comparing the geometry of the Euler wake which is represented by white isosurfaces, and the vortex-lattice wake, which is depicted by a network in grey shades. The direction of the freestream lies in the $x - z$ plane, forming an angle of 12.4° with the positive x–direction.

Fig. 2 shows the flow at $\Psi = 0°$. Vortex sheet and tip vortex of the Euler blade are clearly visible. The position of the two solutions agree in a satisfactory manner, the apparent deviation of the tip vortex after a turn of 180 degrees is due to the fact that it follows the path of the filament leaving the blade tip which is covered by the enrolling lattice. Far in front of the blade the traces of the preceding tip vortex are visible which are highly stretched because of the high cell aspect ratio in this region, thus demonstrating the need for a fine net also in the outer parts of the grid. For further clarification a close-up from another perspective is shown in fig. 3 which uses an isosurface of a higher rotationstrength to cut away secondary features. The structures in the vicinity of the blade can now be explained. First, the inboard vortex can easily be identified below the blade in a position which coincides with the vortex lattice. Second, the reentering tip vortex and its interaction with the preceding vortex sheet is visible.

Fig. 4 illustrates the situation at $\Psi = 120°$. Again the vortex sheet positions coincide, however the roll up of the tip vortex has not yet taken place. This fact is confirmed by the potential solution. The preceding tip vortex enters the domain in the right position and is continuing below the blade following closely the geometry of the vortex lattice. For this case it is known that the main interaction occurs in the range between 0 and 120°, so that the terminal phase is visualized in this figure.

A further confirmation of the good agreement is given in fig. 5 for $\Psi = 240°$. The Euler solution reproduces accurately the vortex structure of the potential method. It also evident that the preceding tip vortex which is generated by the boundary conditions is positioned at the right place.

Solution on reduced grids

Now that the feasibility of the coupling approach has been proved, an attempt to lower the storage and CPU-time requirements by reducing the size of the Euler grid has been made. Numerical studies with grids of different sizes have been carried out, and grid-point savings up to 30% turned out to be possible without accuracy deterioration. The grid on which the following results have been obtained is shown in fig. 6.

For the radial station of $r/R = .9$, the c_p-distribution at 12 azimuthal positions is dipicted in fig. 7. The pressure coefficient is defined as

$$c_p = \frac{p - p_\infty}{\frac{1}{2}\kappa p_\infty \left(M_t \ r/R + M_\infty \sin(\Psi)\right)} \tag{37}$$

A good agreement with the experiment is achieved. In [7] the deviations at $\Psi = 0°$ can be explained by the influence of the rotor shaft at this azimuthal position.

In fig. 8 the time dependency of the normal force coefficient multiplied by Mach number squared during a revolution is plotted. It is calculated with

$$c_n M^2 = \frac{normal force}{\frac{1}{2}\kappa p_\infty \, (local \ chord) \, (length \ unit)} \tag{38}$$

Again, good agreement with the experiment is achieved.

Conclusions

It can be concluded that by imposing free wake data the generation and the transport of the vortices of the preceding blades into the Euler domain can be achieved. Therefore, modeling of multi–bladed rotor flows in the unsteady flight regime is possible by calculating only one blade and taking the others into account by the velocity distribution that they cause on the grid boundaries. Furthermore the farfield boundary can be located closer to the body which results in saving of storage and time. The coupled approach will be investigated in future as a flowfield preconditioner for the chimera technique in order reach faster a periodicity of the solution.

Acknowledgements

Part of this work (the fundamentals of the coupling procedure) was sponsored by the CEC with the project ECARP (AERO-CT-0031/AERO-P2003) ([12], [13]).

References

[1] Eberle, A. : MBB-EUFLEX. A New Flux Extrapolation Scheme Solving the Euler Equations for Arbitrary 3-D Geometry and Speed, Report MBB/LKE122/S/ PUB/140,MBB, Ottobrunn, Germany 1984

[2] Hertel, J. : Euler-Lösungen der stationären Rotorströmung für Schwebe- und den axialen Vorwärtsflug mit Einbeziehung linearer Methoden, PhD thesis, Universität der Bundeswehr München, Neubiberg, 1991

[3] Jameson, A.; Yoon, S. :LU Implicit Schemes with Multiple Grids for the Euler Equations, AIAA-Paper 86-0105, presented at AIAA 24th Aerospace Sciences Meeting, Reno, Nevada, January 6-9, 1986

[4] Krämer, E. : Theoretische Untersuchungen der stationären Rotorblattumströmung mit Hilfe eines Euler-Verfahrens, PhD thesis, Universität der Bundeswehr München, VDI Fortschrittsberichte, Reihe 7: Strömungstechnik, Nr. 197, VDI-Verlag, Düsseldorf 1991

[5] Krämer, E.; Hertel, J.; Wagner, S.: Computation of Subsonic and Transonic Helicopter Rotor Flow Using Euler Equations, Proceedings of the 13th European Rotorcraft Forum, Arles, Paper no. 2-14, 1987

[6] Kroll, N. : Computation of the Flow Fields of Propellers and Hovering Rotors Using Euler Equations, Proceedings of the 12th European Rotorcraft Forum, Garmisch-Partenkirchen, Paper no. 28, 1986

[7] Pahlke, K.; Sides, J.; Wehr, D. : Two- and Three-Bladed ONERA Model Rotors, in: ECARP: European Computational Aerodynamics Research Project II: Validation of CFD Codes and Assessment of Turbulence Models, chapter III.10, Edited by: W. Haase, E. Chaput, E. Elsholz, M.A. Leschziner, U.R. Mueller, Notes on Numerical Fluid Mechanics, Vieweg Verlag, to be published

[8] Rieger, H.; Jameson, A. : Solution of Steady Three-Dimensional Compressible Euler and Navier-Stokes Equations by an Implicit LU Scheme, AIAA Paper 88-0619, January 1988

[9] Stangl, R.; Wagner, S. : Euler-Calculation of the Flow Field around a Helicopter Rotor in Forward Flight, Proceedings of the 20th European Rotorcraft Forum, Paper no. 38, Amsterdam, 1994

[10] Stangl, R.; Wagner, S. : Euler Method to Calculate the Flow around a Helicopter Using a Chimera Technique, Proceedings of the 52nd AHS Forum, p. 453-462, Washington D.C, 1996

[11] Zerle, L.; Wagner, S.: Final Technical Report BRITE EURAM Aero 0011 C(A) 'SCIA' Project 1990-1992, Technical report, Institut für Luftfahrttechnik und Leichtbau, Universität der Bundeswehr München, Neubiberg, 1992

[12] Wehr, D.; Zerle, L.; Wagner, S.: Improvement of efficiency and robustness of unsteady Euler codes for 3D time accurate calculations, in: ECARP: European Computational Aerodynamics Research Project II: Validation of CFD Codes and Assessment of Turbulence Models, chapter II.28, Edited by: W. Haase, E. Chaput, E. Elsholz, M.A. Leschziner, U.R. Mueller, Notes on Numerical Fluid Mechanics, Vieweg Verlag, to be published

[13] Wehr, D.; Stangl, R.; Uhl, B.; Wagner, S.: Calculations of rotors in unsteady forward flight using potential and Euler methods, in: ECARP: European Computational Aerodynamics Research Project II: Validation of CFD Codes and Assessment of Turbulence Models, chapter II.29, Edited by: W. Haase, E. Chaput, E. Elsholz, M.A. Leschziner, U.R. Mueller, Notes on Numerical Fluid Mechanics, Vieweg Verlag, to be published

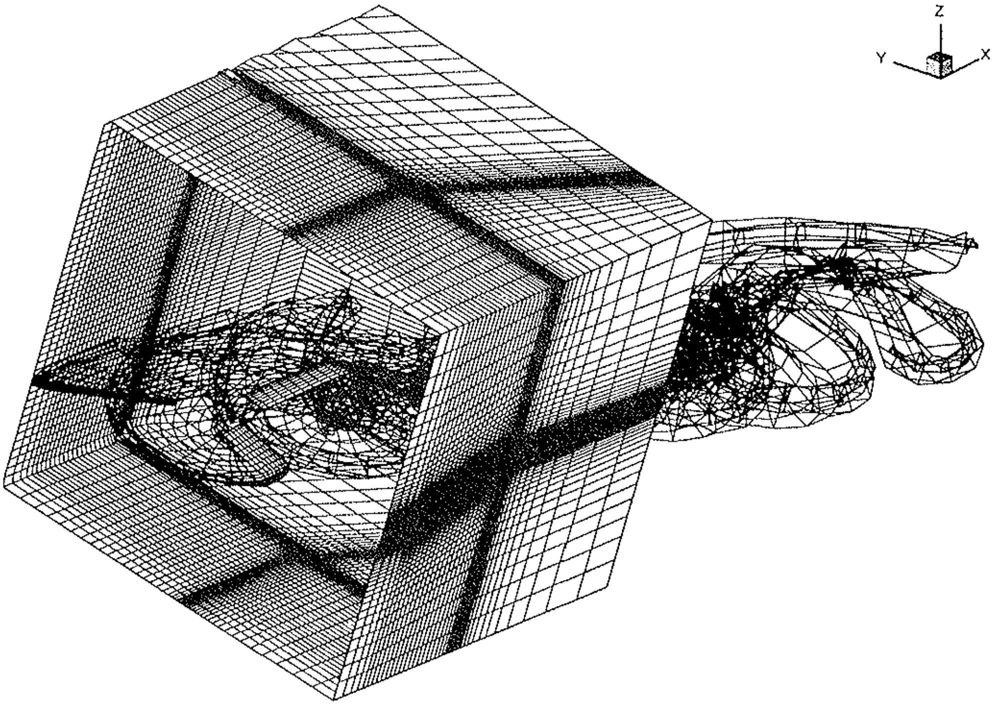

Figure 1: Example of output of vortex-lattice code and dimensions of Euler grid for rotor calculations

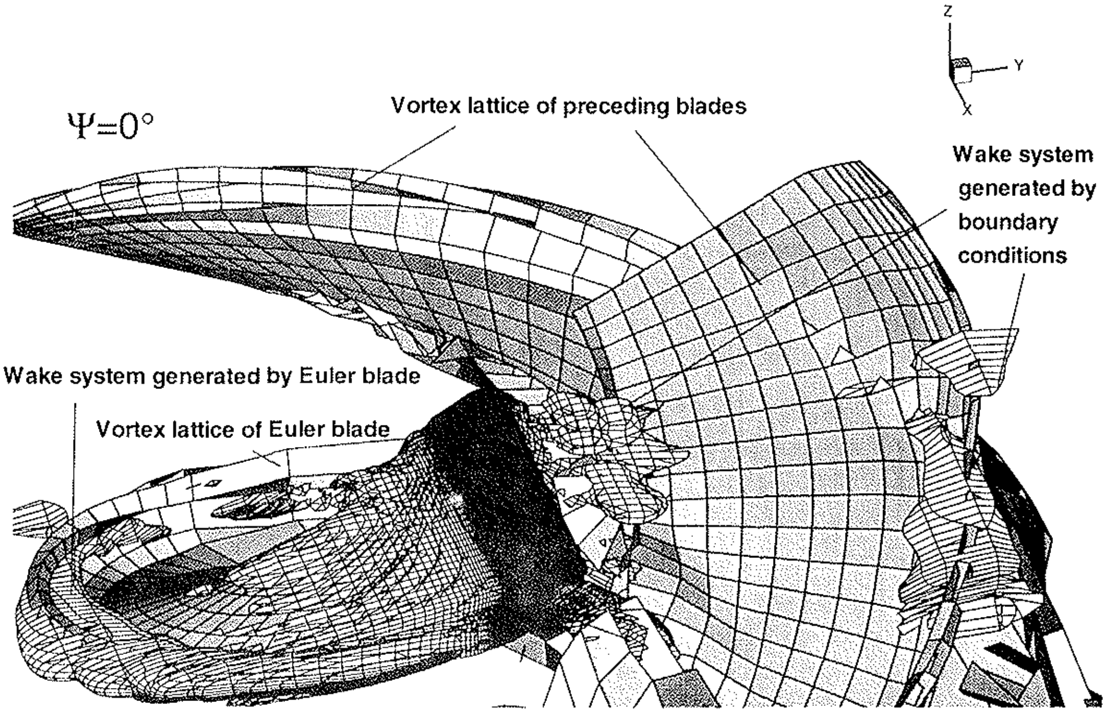

Figure 2: Wake system at $\Psi = 0°$

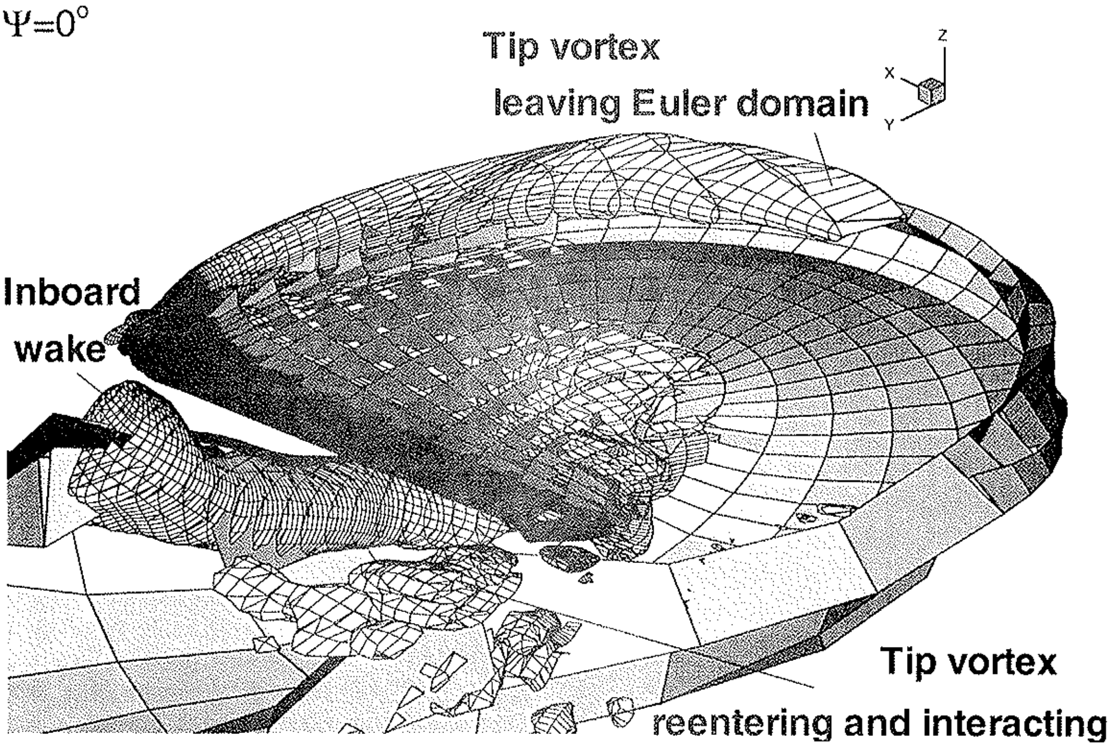

Figure 3: Detail of wake system at $\Psi = 0°$

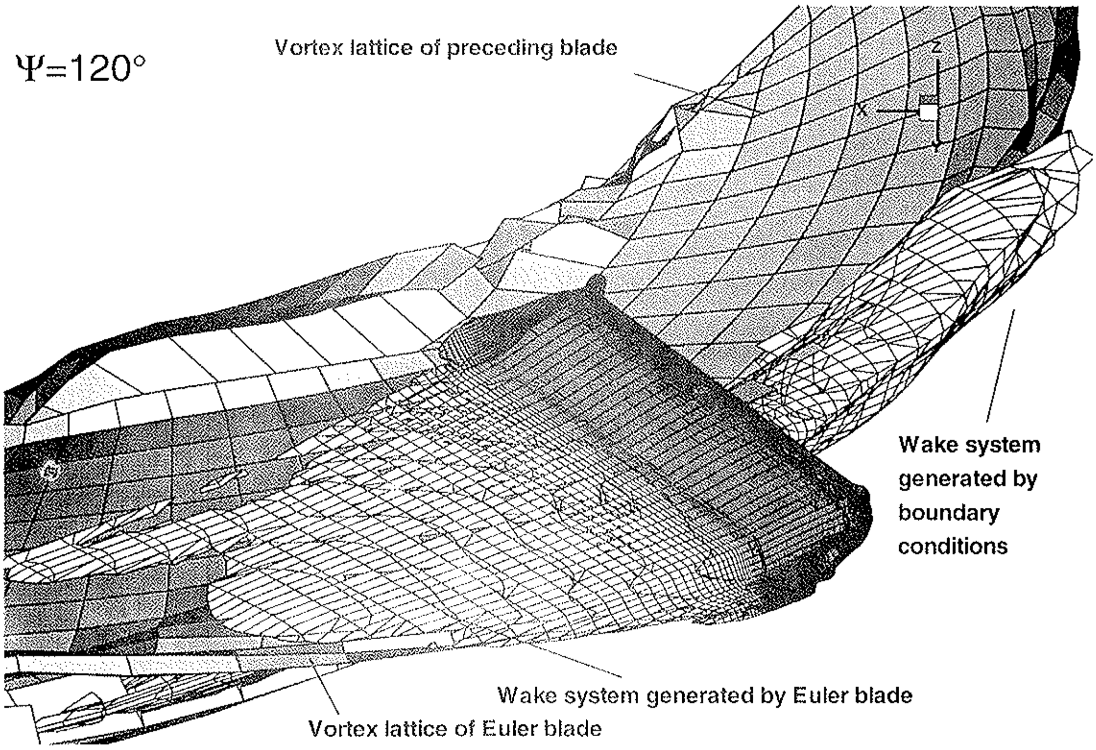

Figure 4: Wake system at $\Psi = 120°$

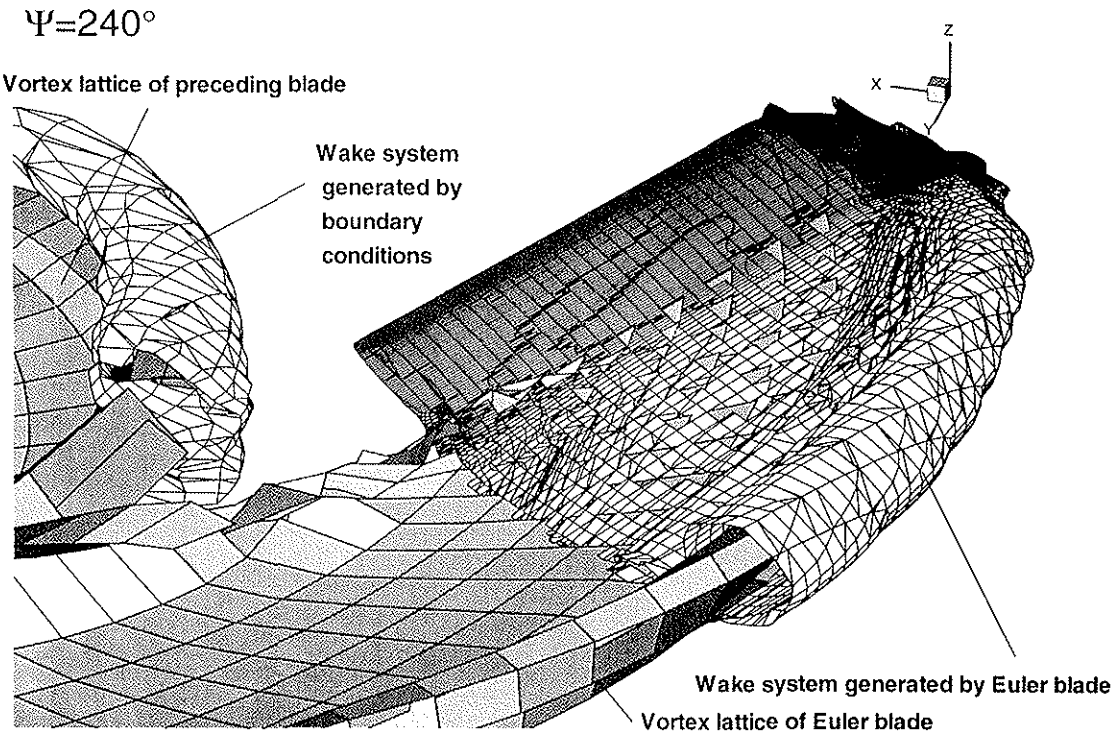

Figure 5: Wake system at $\Psi = 240°$

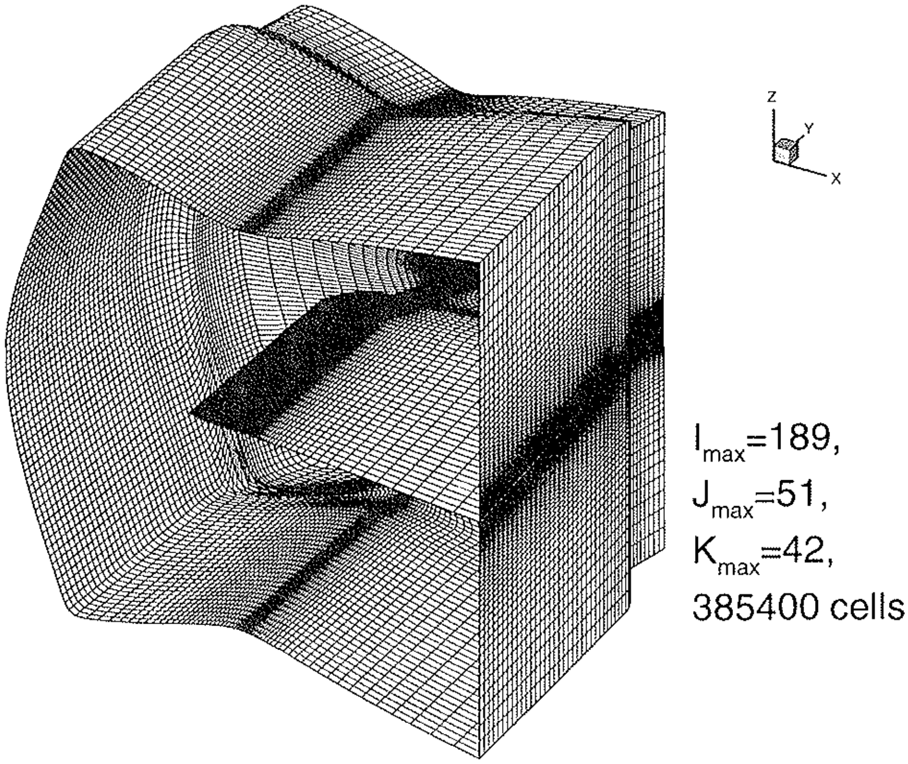

Figure 6: Grid of reduced size

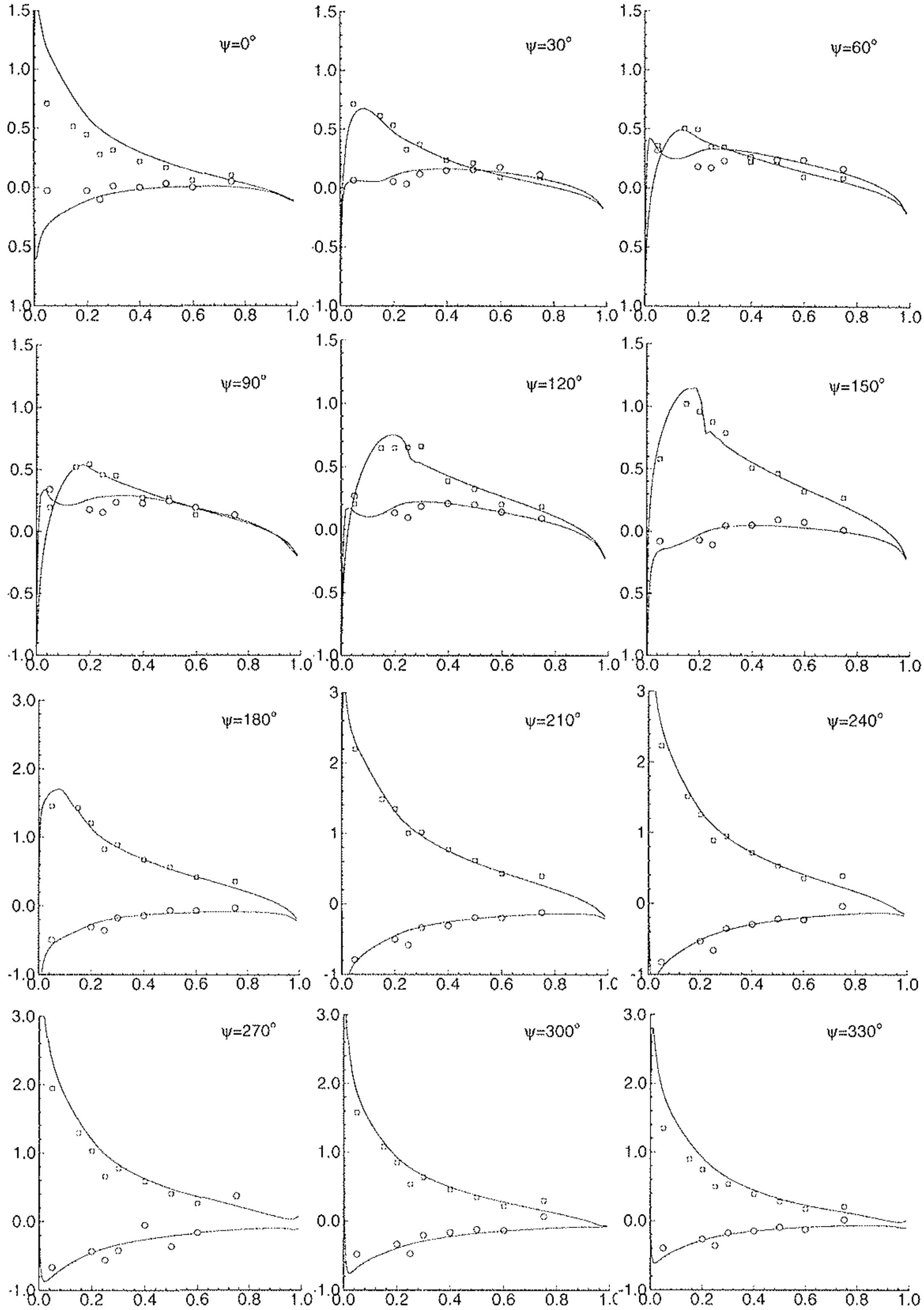

Figure 7: $-C_p$ versus x/c at r/R=.9 for different azimuth angles, (□, ○ : experimental values for upper and lower side from [7])

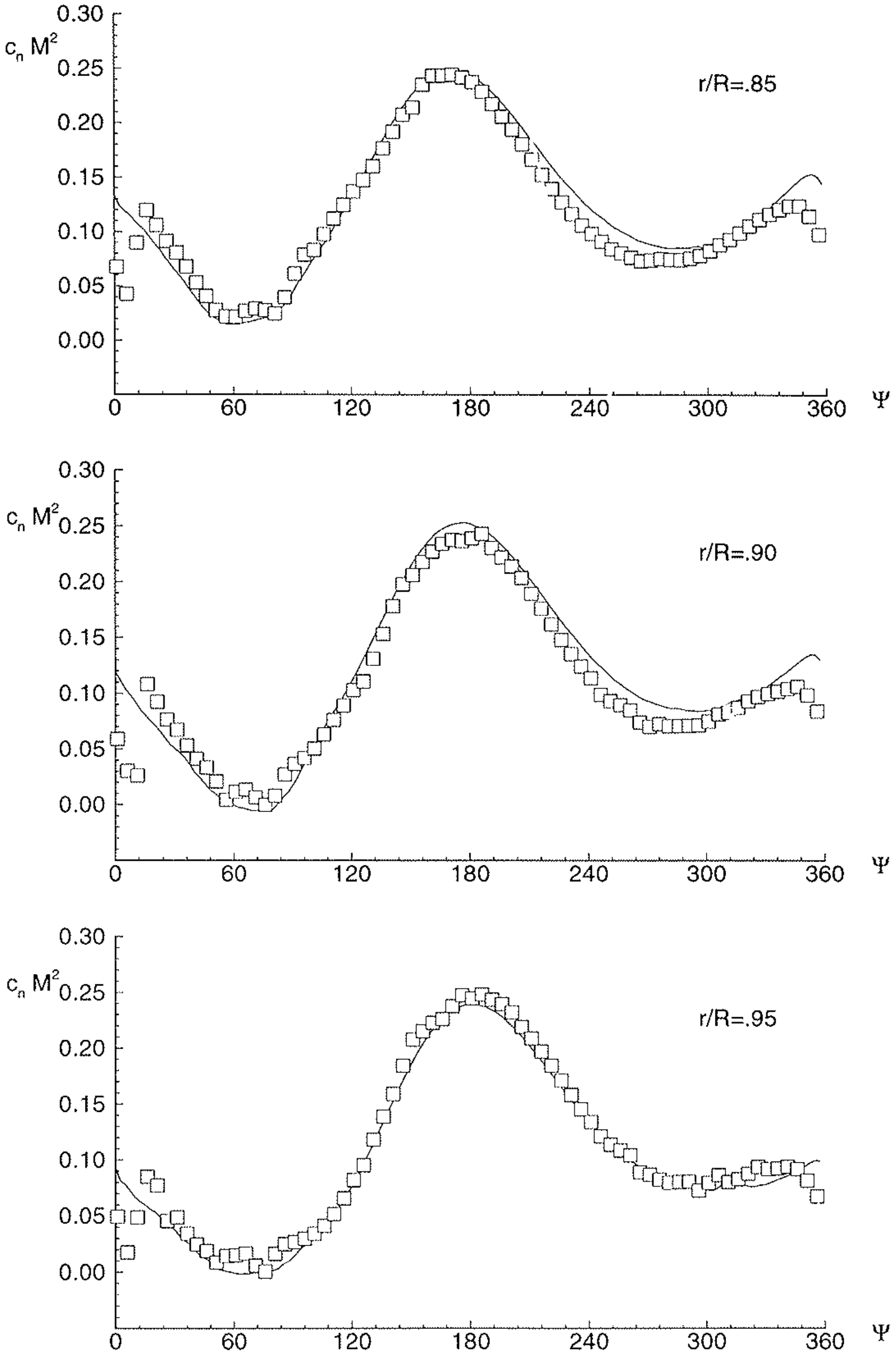

Figure 8: Normal force coefficient as function of azimuth angle, (□: experimental values from [7])